Computational Optical Scanning Holography

Yoneda, Naru
Liu, Jung-Ping
Matoba, Osamu
Saita, Yusuke
Nomura, Takanori

(Citation)
Photonics,11(4):347

(Issue Date)
2024-04

(Resource Type)
journal article

(Version)
Version of Record

(URL)
https://hdl.handle.net/20.500.14094/0100489407

photonics

MDPI

Review

Computational Optical Scanning Holography

Naru Yoneda [1,2,*], Jung-Ping Liu [3,4], Osamu Matoba [1,2], Yusuke Saita [5] and Takanori Nomura [5]

1 Graduate School of System Informatics, Department of System Science, Kobe University, Rokkodai 1-1, Nada, Kobe 657-8501, Japan; matoba@kobe-u.ac.jp
2 Center for Optical Scattering Image Science, Kobe University, Rokkodai 1-1, Nada, Kobe 657-8501, Japan
3 Department of Photonics, Feng Chia University, 100 Wenhwa Rd., Seatwen, Taichung 40724, Taiwan; jpliu@fcu.edu.tw
4 Digital Optics Center, Feng Chia University, 100 Wenhwa Rd., Seatwen, Taichung 40724, Taiwan
5 Faculty of Systems Engineering, Wakayama University, 930 Sakaedani, Wakayama 640-8510, Japan; saita@wakayama-u.ac.jp (Y.S.); nom@wakayama-u.ac.jp (T.N.)
* Correspondence: yoneda.naru@port.kobe-u.ac.jp; Tel.: +81-78-803-6240

Abstract: Holographic techniques are indispensable tools for modern optical engineering. Over the past two decades, research about incoherent digital holography has continued to attract attention. Optical scanning holography (OSH) can obtain incoherent holograms using single-pixel detection and structured illumination with Fresnel zone patterns (FZPs). Particularly by changing the size of a detector, OSH can also obtain holograms under coherently illuminated conditions. Since 1979, OSH has continuously evolved. According to the evolution of semiconductor technology, spatial light modulators (SLMs) come to be useful for various imaging fields. By using SLM techniques for OSH, the practicality of OSH is improved. These SLM-based OSH methods are termed computational OSH (COSH). In this review, the configurations, recording and reconstruction methods, and proposed applications of COSH are reviewed.

Keywords: digital holography; optical scanning holography; single-pixel imaging

Citation: Yoneda, N.; Liu, J.-P.; Matoba, O.; Saita, Y.; Nomura, T. Computational Optical Scanning Holography. *Photonics* **2024**, *11*, 347. https://doi.org/10.3390/photonics11040347

Received: 7 March 2024
Revised: 1 April 2024
Accepted: 8 April 2024
Published: 10 April 2024

1. Introduction

With the advancement of semiconductor technology and information science, imaging methods beyond classical optical techniques, termed computational imaging, have been proposed [1]. In particular, single-pixel imaging (SPI), one of the computational imaging techniques, can be applied to various conditions where an image sensor is not applicable [2]. SPI is anticipated to be an imaging technology in wavelength regions where the imaging sensors have not advanced compared with the broader wavelength band of the used sensors [3–7]. Additionally, the use of highly sensitive photodetectors such as photomultiplier tubes and avalanche photodiodes as detectors allows applications in low-photon conditions [8,9]. In addition, SPI possesses the advantage of high resilience against disturbances like scattering and aberrations [10,11].

Against this background, various SPI techniques have been proposed, including ghost imaging (GI) [12], computational GI (CGI) [13], Hadamard transform imaging (HTI) [14], and Fourier single-pixel imaging (FSI) [15]. Optical scanning holography (OSH) is also one of the SPI techniques which utilizes Fresnel zone patterns (FZPs), or interference fringes with different curvatures, as structured illumination [16,17]. As the size of the FZP changes according to light propagation, three-dimensional information is encoded in the intensities obtained by a single-pixel detector. In OSH, multiple-wavelength imaging [18], sectioning imaging [19–22], stereo lighting reconstruction [23], edge extraction [24], axial localization [25], cryptography [26], resolution enhancement [27,28], remote sensing [29], and recording of phase holograms have been proposed. In terms of holography, OSH can be categorized as incoherent digital holography (IDH) [30]. The time to obtain holograms of OSH is limited by the scanning speed of the FZP due to single-pixel detection [31],

although recent IDH techniques with an image sensor can record moving targets with the framerate [32–34]. While OSH possesses the disadvantage of low measurement speeds, many kinds of undersampling methods have been proposed [35–38]. Interestingly, OSH also obtains holograms under a coherently illuminated condition by using a pinhole in front of a detector [39–42]. However, the optical set-up of OSH is based on the two-beam interferometer and is significantly affected by disturbances such as vibrations. The need for 2D scanning with a galvanometer mirror and a phase shifter to shift the phase of the FZP makes the optical system complicated.

To partially address these challenges, a method using a geometric phase lens was proposed [43,44]. This method employs lenses that change the curvature of outgoing waves based on the circular polarization of the incident light, enabling the realization of FZP in a single optical path. However, a 2D scanner and a phase shifter are still required. To alleviate the complexity of the optical system in OSH, motionless OSH (MOSH) [45] and interferenceless OSH (IOSH) [46] have been proposed. These approaches use a spatial light modulator (SLM) to generate structured illumination patterns and can be implemented with the same optical systems as HTI, FSI, and CGI. This paradigm shift is similar to the evolution from thermal GI to CGI. For this reason, these two methods are termed computational OSH (COSH).

In this paper, we summarize the recent progress of research on COSH. In the following chapters, recent research trends related to COSH will be introduced, including the basic principles of general OSH, MOSH, and IOSH in Section 2. Analysis of the methods is performed in Section 3, followed bt application examples in the optical system of COSH in Section 4 and finally the concluding remarks for this paper in Section 5.

2. Systems

2.1. Basic Concept of Conventional OSH

To begin with, we will first introduce the set-up and principles of conventional OSH, which has been well studied for more than three decades. Figure 1 depicts the schematic set-up of conventional OSH. An electro-optic modulator (EOM) is applied as the frequency shifter in the system, but other frequency-shifting devices, such as an acousto-optic modulator, can be also applied to build a conventional OSH system. In Figure 1, the laser beam is first modulated by an EOM, and then the two modes of polarized light are separated by a polarizing beamsplitter (PBS). The two pupils in the interferometer significantly affect the properties of the system, which can find applications in imaging with various filtering effects [28,47–50]. For typical imaging, the two beams are manipulated to become a plane wave and a spherical wave, respectively, and are recombined by a beamsplitter (BS). The two beams are projected to the object space by Lens 3, forming a 3D, time-varying interference fringe called a time-dependent Fresnel zone plate (TDFZP). In the paraxial approximation, the TDFZP is represented by

$$\begin{aligned}\mathrm{TDFZP}(x,y,z,t) &= \left|A_p + A_s \exp\left\{\frac{ik}{2z}(x^2+y^2) + i(\phi - \Omega t)\right\}\right|^2 \\ &= |A_p|^2 + |A_s|^2 + 2|A_p||A_s|\cos\left\{\frac{k}{2z}(x^2+y^2) + \phi - \Omega t\right\}, \end{aligned} \quad (1)$$

where A_p and A_s are the amplitudes of the plane wave and the spherical wave, respectively. k is the wave number, ϕ is the initial phase of the spherical phase, and the angular frequency is introduced by the EOM. As shown in Figure 2a, the transverse fringe density of the TDFZP is inversely proportional to the axial distance (z). Therefore, as the object mounted on an x-y stage is raster scanned by the TDFZP, its 3D profile can be coded to the scattered light and detected by the photodetector PD 1. In addition, the phase of the interference fringe continuously changes because of the use of the EOM, as shown in Figure 2b. The temporal oscillation features easy extraction of the initial phase by using, for example, a lock-in amplifier. This is essential to remove the annoying zero-order light and the twin

image in the conventional OSH. Accordingly, another photodetector (PD 2) is set on the other arm of the interferometer to produce the reference for high-accuracy phase detection.

The spatial coherence of the OSH system depends on the detection scheme, which is another important feature of OSH [41,42,51]. If PD 1 in Figure 1 is a point-like photodetector, then the OSH system is operated in the coherent mode, and the complex hologram acquired from the lock-in amplifier can be expressed as

$$H_{co}(x,y) = \int_z o(x,y,z) \otimes h(x,y;z)dz, \tag{2}$$

where $o(x,y,z)$ is the amplitude transmittance of the object, "$\otimes$" is the operator of 2D convolution, and

$$h(x,y;z) = \exp\left[\frac{ik}{2z}(x^2+y^2)\right]. \tag{3}$$

is the impulse response of the system. On the other hand, the OSH is operated in the incoherent mode if PD 1 is a bucket detector. The corresponding hologram formula is

$$H_{inco}(x,y) = \int_z I(x,y,z) \otimes h(x,y;z)dz, \tag{4}$$

where $I(x,y,z)$ is the intensity transmittance of the object. It should be noted that in either the coherent mode or the incoherent mode, the scanning hologram can be reconstructed by using the same impulse response. Explicitly, the reconstructed field of an incoherent scanning hologram is

$$E_{inco}(x,y;z_r) = H_{inco}(x,y) \otimes h(x,y;z_r), \tag{5}$$

where z_r is the reconstruction distance.

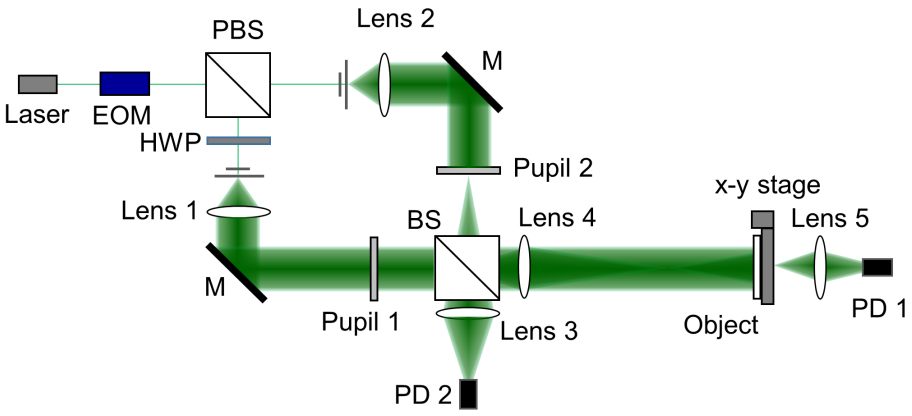

Figure 1. The set-up of conventional OSH. EOM = electro-optic modulator; PBS = polarizing beam-splitter; HWP = half-wave plate; M = mirror; BS = beamsplitter; PDs = photodetectors.

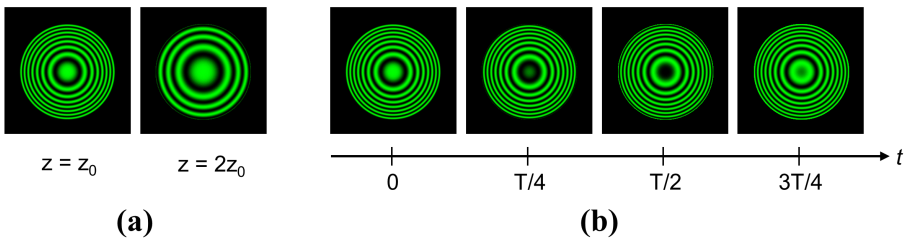

Figure 2. The TDFZP at different depths (**a**) and different times (**b**).

2.2. Motionless OSH

One of the methods for realizing COSH is MOSH [45]. MOSH utilizes the birefringence of a liquid crystal-type SLM (LC-SLM) to generate FZPs. The conceptual diagram of MOSH is illustrated in Figure 3. This principle was inspired by Fresnel incoherent correlation holography [52], which is one of the incoherent digital holography techniques. The principle of generating FZPs using an LC-SLM is based on the principles of common path polarization interferometers [53].

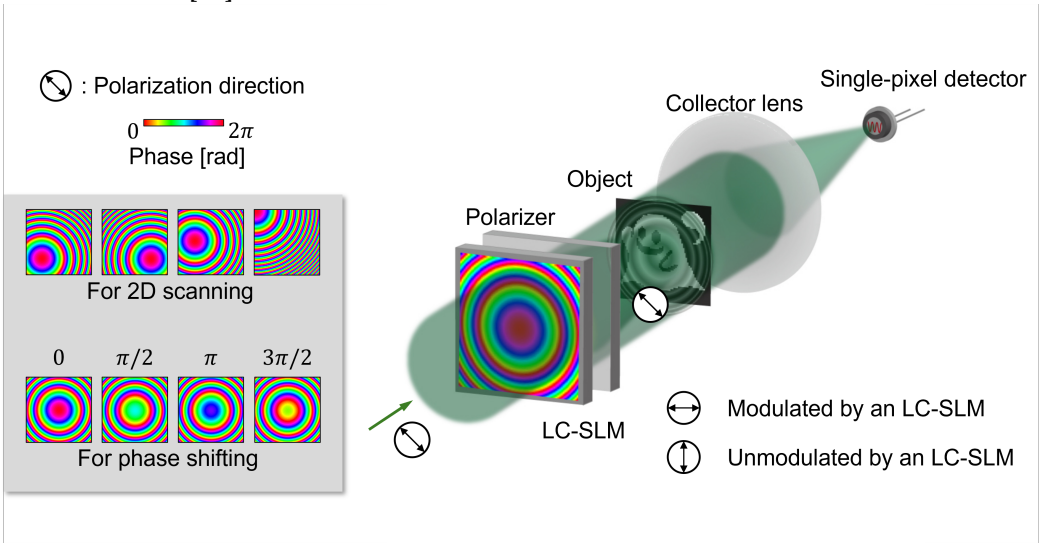

Figure 3. Conceptual diagram of MOSH.

In MOSH, a diagonally polarized plane wave is incident on the LC-SLM. The SLM displays the phase distribution of a spherical wave. The light from the SLM is split into two components due to its birefringence. The light with the polarization direction modulated by the SLM becomes a spherical wave, while the unmodulated light remains a plane wave. Subsequently, these orthogonally polarized waves pass through a polarizer. By setting the transmission axis of the polarizer at a diagonal angle, interference between the spherical and plane waves occurs on the object plane, resulting in the generation of FZPs. The FZP generated by MOSH's configuration can be described as follows:

$$\begin{aligned}\mathrm{FZP}_{\phi}(x,y;z) =& \left| A_h + A_v \exp\left\{ \frac{ik}{2z}(x^2+y^2) + \phi \right\} \right|^2 \\ =& |A_h|^2 + |A_v|^2 + 2|A_h||A_v| \cos\left\{ \frac{k}{2z}(x^2+y^2) + \phi \right\}, \end{aligned} \tag{6}$$

where A_h and A_v are the polarization components of the incident light along the horizontal and vertical directions, respectively, while ϕ is the bias phase of the spherical phase distributions. In addition, by changing the center position of the phase distribution of a spherical wave, 2D scanning is achieved. Meanwhile, by changing the initial phase ϕ, phase shifting is also realized by the same SLM.

The proof-of-principle experiment of MOSH was conducted using the optical system shown in Figure 4. The light source was a green fiber laser (MPB Communications, Inc., VFL-P-500). The collimated beam sent through a spatial filter illuminated an SLM (Hamamatsu Photonics K.K. X13138-01). The center region of the SLM with 128 × 128 pixels was used for displaying the spherical phase distributions. The light from the SLM was projected onto an object with a 4 f optical set-up composed of lenses 2 and 3. The transmitted beam was Fourier transformed by lens 4 and detected by a photodiode (Hamamatsu K.K. C10439-03). The measured signals were quantized by a 16 bit analog-to-digital converter (Hamamatsu K.K. C10475). In MOSH, the phase distribution of a spherical wave is displayed on the SLM to generate the FZP. Therefore, it is necessary to discretely represent the phase distribution

of the spherical wave, and errors may occur if the sampling theorem is not satisfied. The effect of the phase distribution displayed on the SLM was evaluated in [54]. This evaluation illustrates that the spatial resolution of MOSH is determined by the pixel pitch of the SLM and the sampling condition of the phase distribution of the spherical wave on the SLM plane. Consequently, carefully selecting the phase distribution displayed on the SLM is crucial to match the target object in MOSH. Additionally, the imaging speed in MOSH is constrained by the refresh rate of the SLM. Since the typical refresh rate of LC-SLMs is 60 Hz, it takes about 18 min to obtain a reconstructed distribution of 128 × 128 pixels.

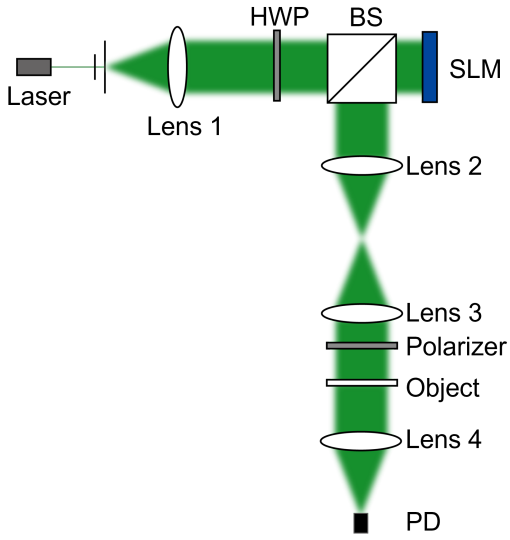

Figure 4. Optical set-up of MOSH for proof-of-principle experiments. HWP = half-wave plate; BS = beamsplitter; PD = photodiode.

Note that the noise in MOSH depends on the quality of the used LC-SLM, since the intrinsic polarization of the SLM and the operation speed of the liquid crystal affect the quality of the generated FZP.

2.3. Interferenceless OSH

In conventional OSH, the scanning beam is produced by interference, which makes the system expensive and bulky. In addition, the system is easily disturbed by environmental fluctuations. For these reasons, the concept of interferenceless optical scanning holography (IOSH) arose [46,55]. Figure 5 depicts the schematic set-up of IOSH. The laser beam is collimated and directed to a digital micromirror device (DMD) via a total internal reflection prism (TIRP). The DMD is a high-speed SLM. By controlling the angle of its elemental micro mirrors, the incident light can be reflected either normally (on) or at a high angle (off). In this way, binary patterns can be displayed by the DMD at as high as a 30 kHz frame rate. This is also the main reason why a DMD instead of a LC-SLM is applied in IOSH. In IOSH, the interference fringe is directly displayed on the DMD and projected onto the object by Lens 2. The photodetector PD behind the object is applied to detect the scattered object light. Being similar to MOSH, the scanning in IOSH can be realized by shifting the location of the interference fringes displayed on the DMD. Meanwhile, the initial phase of the interference fringes is periodically changed, becoming like what is observed in conventional OSH (Figure 2b). In this way, the holographic recording can be 100 times faster than that of MOSH. On the other hand, IOSH can also be realized by mechanical scanning or digital-mechanical hybrid scanning [46]. The horizontal scanning is performed digitally, while the vertical scanning is performed by moving the y axis stage. Both the memory of the DMD system and the ability of 3D imaging can benefit from this method. One of the problems of IOSH is that the projection lens can only produce a clear fringe image within the depth of field. The fringe image at the plane outside the depth

of field blurs because of defocusing. To solve this problem, the point spread functions (PSFs) at different planes of the object space are preliminarily recorded experimentally, using a pinhole as the specimen. Figure 6 shows the real part of three PSFs at various planes. It is noted that the vertical size of the PSF is proportional to the depth (image distance) of the pinhole plane. The reason for this is that the magnification of the fringe image is proportional to the image distance. On the other hand, the horizontal sizes of the PSFs are almost the same because the horizonal sampling is performed digitally, and hence the horizonal pixel pitch is proportional to the image distance too. As both the horizontal image size and horizontal pixel pitch are proportional to the image distance, the full horizontal size of the PSF in pixels remains the same at different image distances. It should be noted that anisotropic magnification at different depths associated with the hybrid scanning technique enhances the depth resolution of IOSH.

In the reconstruction, the experimental PSFs instead of the theoretical impulse response is applied in Equation (5). By using the experimental PSFs, the aberrations can mostly be compensated for. One example of IOSH is shown in Figure 7. The object was a mini block with a size of 4 mm × 16 mm × 32 mm. The hologram size was 600 × 800 pixels, with a pixel pitch of 23 μm. As the hologram was reconstructed with the experimental PSF at 200 mm, the reconstructed image showed clear details (Figure 7b). This experimental result proves the 3D imaging ability of IOSH.

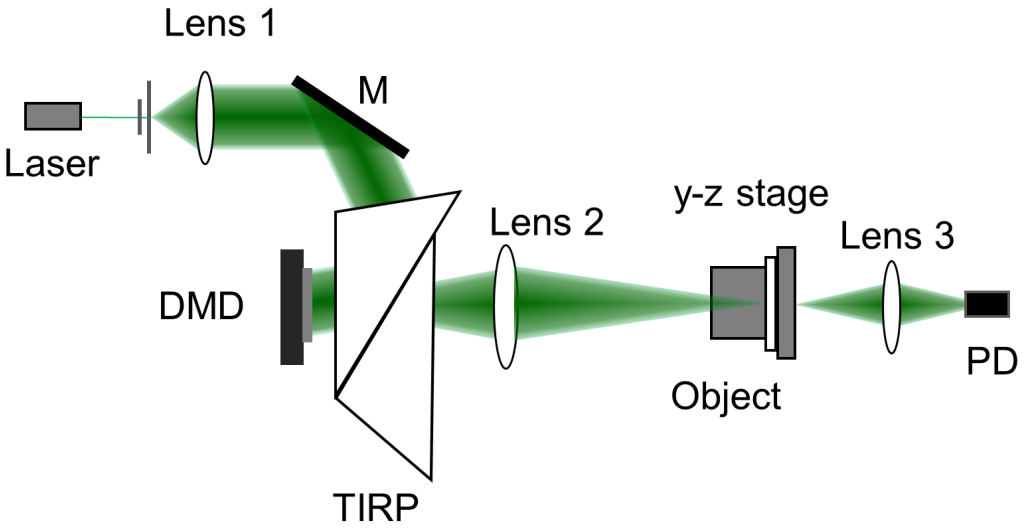

Figure 5. Set-up of interferenceless optical scanning holography. M = mirror; TIRP = total internal reflection prism.

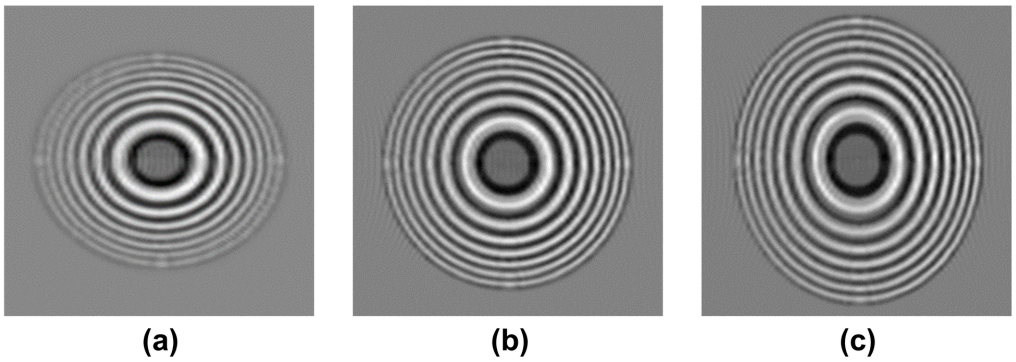

Figure 6. Real part of experimental PSFs at image distances of 180 mm (**a**), 190 mm (**b**) and 200 mm (**c**). The image plane of the projection lens is at 190 mm.

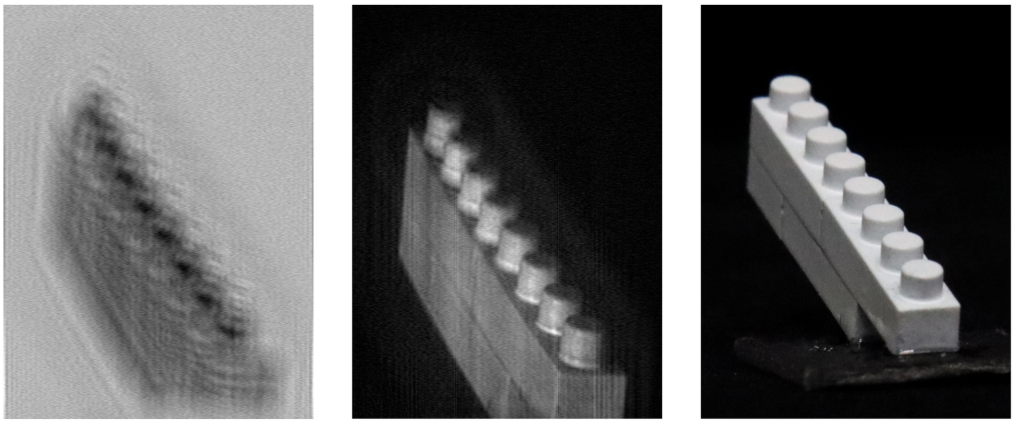

Figure 7. Experimental demonstration of IOSH. (**a**) The real part of the acquired complex hologram by IOSH. (**b**) The reconstructed image. (**c**) Photo of the object.

2.4. Comparison of OSH and COSH

In this subsection, we compare the characteristics of OSH and COSH. The comparison of features is summarized in Table 1. The first difference between OSH and COSH is the complexity of the optical system, since OSH requires a two-axis interferometer, a phase shifter, and a two-dimensional scanner. On the other hand, the spatial resolution of the FZP is limited by the pixel pitch of the SLM in COSH, but conventional OSH can achieve a high spatial resolution via fine sampling. As for the imaging speed, OSH can use a high-speed two-dimensional scanner. Therefore, the imaging speed of OSH is usually higher than that of COSH. Nevertheless, it should be remembered that there is always a trade-off between the spatial resolution and the scanning speed for either COSH or OSH. Finally, the simplicity of the optical system makes COSH more flexible for various applications.

Table 1. Comparison of OSH and COSH.

	OSH	**COSH**
Complexity	High	Low
Speed	High	Low
Spatial resolution	High	Low
Application flexibility	Low	High

Note that there is no particular restriction on the illumination wavelength width in COSH. However, in the case of MOSH, the phase shift error is smaller when the illumination wavelength width is smaller because of the wavelength-dependent characteristics of the SLM. This could be mitigated by applying a generalized phase shift method [56]. In the case of IOSH, the wavelength of the illumination depends on the mirror coating of the DMD, and thus the reflectance may affect the reconstructed image. Since the use of multiple wavelengths for illumination has been proposed for OSH [18], it is possible to achieve multi-wavelength imaging in COSH by considering these features.

3. Analysis Methods

3.1. Spatially Divided Phase-Shifting Method

In digital holography using an image sensor, parallel phase-shifting digital holography has been proposed, where holograms with different phase shift amounts are simultaneously recorded [57–60]. This approach enables the acquisition of holograms with different phase shift amounts in a single shot, and holograms can be acquired at the frame rate of the imaging sensor. By dividing the obtained hologram on a per pixel basis and performing interpolation, the necessary holograms for phase-shifting techniques can be simultaneously

acquired. Parallel phase-shifting digital holography can be applied for recording high-speed phenomena such as gas flow [61] and sound field imaging [62].

If the idea of parallel phase-shifting holography can be applied to COSH, hten it has the potential to reduce the measurement time in COSH.

In MOSH, a spatially divided phase-shifting (SDPS) method was proposed in [54] to achieve parallel phase shifting (named SP-MOSH in [54]). SP-MOSH is realized by simultaneously changing the spatial position and initial phase of the FZP. The conceptual diagram of SP-MOSH is shown in Figure 8.

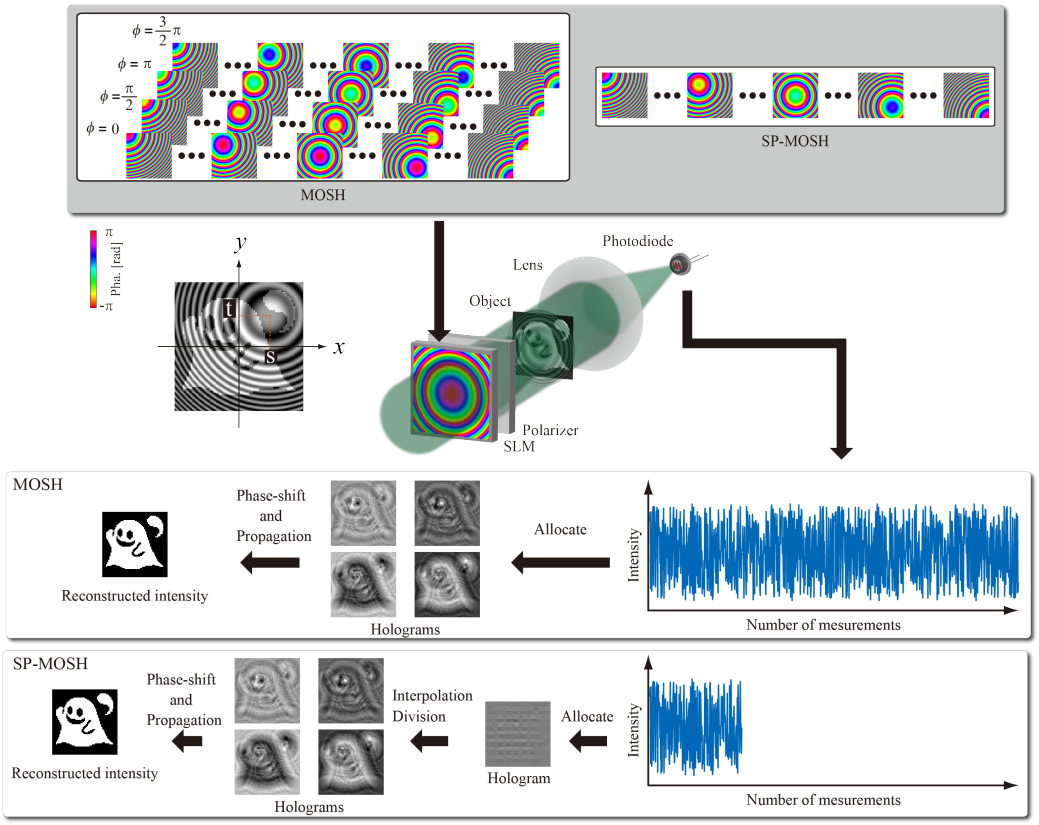

Figure 8. Comparison of detection and reproduction processes of MOSH and SP-MOSH. Reprinted with permission from [54]. © Optica Publishing Group.

The hologram obtained through this process is almost identical to what is obtained in digital holography using an image sensor. Applying the same reconstruction process allows the acquisition of the necessary phase-shifting holograms with only the number of measurements equal to the number of pixels. The authors of [54] experimentally demonstrated the capability to acquire the phase-shifting holograms required for the four-step phase-shifting method. The optical system is the same as that in Figure 4, with the only modification being that the FZP is displayed on the SLM. The results obtained through conventional MOSH and SP-MOSH are presented in Figure 9. In SP-MOSH, due to the inherent trade-off between the spatial bandwidth and temporal resolution, there is a challenge in achieving a high spatial resolution, resulting in an intensity distribution at the defocus position different from that of conventional MOSH results. Therefore, SP-MOSH is effective when the temporal resolution is more crucial than the spatial resolution.

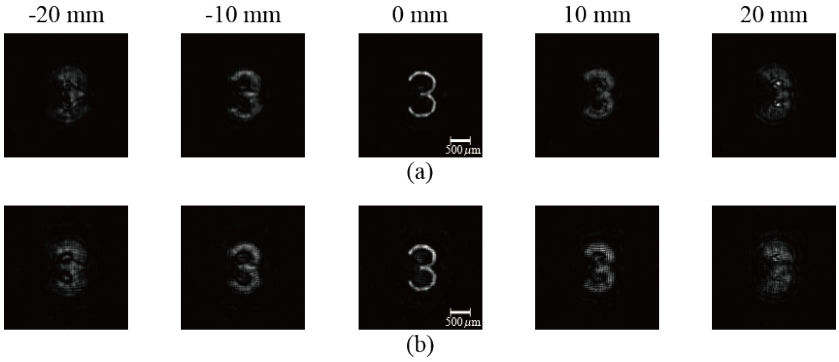

Figure 9. Intensity distributions reconstructed by (**a**) original MOSH and (**b**) SP-MOSH. Reprinted with permission from [54]. © Optica Publishing Group.

3.2. Two-Step Spatially Divided Phase-Shifting Method

One problem with SDPS is its lower spatial resolution compared with conventional COSH. To address this issue, the two-step phase-shifting method [63] was introduced to SDPS [64]. The conceptual diagram of this method is shown in Figure 10.

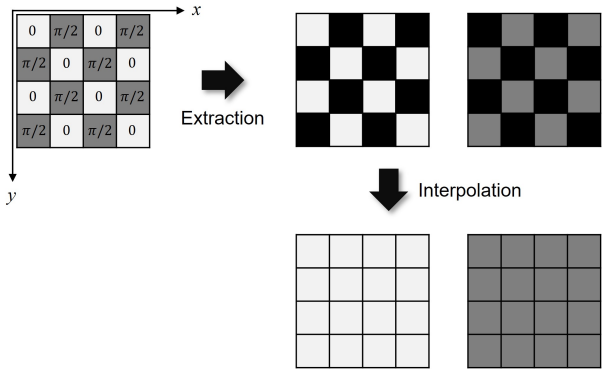

Figure 10. Schematic of spatially divided two-step phase-shifting method. The black pixel value is interpolated by the pixel values to the top, bottom, left, and right of it. Reprinted with permission from [54]. © IOP Publishing.

In this approach, holograms with phase shift amounts of 0 and $\pi/2$ are obtained by simultaneously varying the spatial position and phase of the FZP, similar to SP-MOSH. Through this process, holograms with phase shift amounts of 0 and $\pi/2$ are obtained via hologram division and interpolation. Typically, to acquire the complex amplitude distribution from two holograms, some algorithm is required to remove the bias component present in the hologram [65–67]. The two-step phase shift-based SDPS in COSH addresses this problem by utilizing information from the object's intensity sum to obtain the bias component in the hologram [64]. Therefore, the number of measurements in this method is N + 1, where N is the number of pixels, with the additional measurement aimed at acquiring the intensity sum from the object. Displaying a uniform distribution on an SLM or a DMD allows obtaining the intensity sum of the object.

The experimental results comparing conventional SDPS and 2-step phase-shifting-based SDPS are presented in Figure 11. The results indicate an improvement in the spatial resolution with the two-step phase-shifting method. Furthermore, a simulation comparing the results of conventional SDPS and two-step phase shifting-based SDPS under noisy conditions is shown in Figure 12. When using a rectangular aperture as the object and evaluating the coefficient of variance (CV), the simulation results suggest that conventional SDPS exhibits better noise resistance, as shown in Table 2. This aligns with the general result that the large number of holograms for phase-shifting methods enhances their robustness against noise.

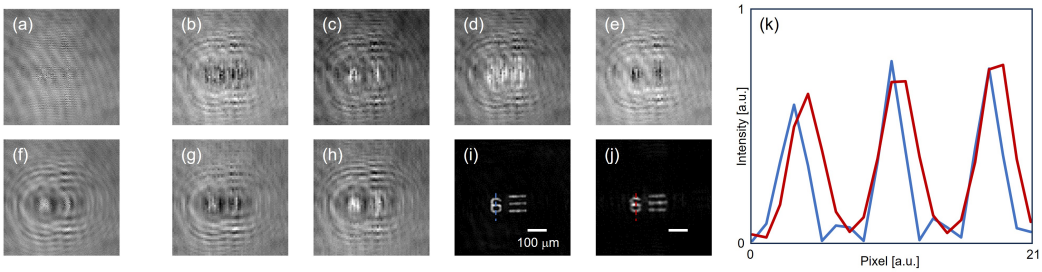

Figure 11. Experimental results for (**a**) spatially divided 4 step phase-shifted hologram, (**b**–**e**) interpolated phase-shifted holograms from (**a**,**f**) with spatially divided 2 step phase-shifted hologram, (**g**,**h**) interpolated phase-shifted holograms from (**f**,**i**) with reconstructed intensity distribution of S2P, and (**j**) reconstructed intensity distribution of S4P and sectional profiles at broken lines in (**i**,**j**). Reprinted with permission from [54]. © IOP Publishing.

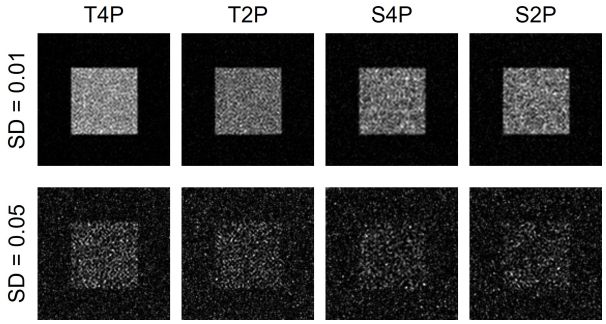

Figure 12. Reconstructed intensity distributions under noisy conditions. T4P = temporal 4 step phase shifting; T2P = temporal 2 step phase shifting; S4P = spatially divided 4 step phase shifting; S2P = spatially divided 2 step phase shifting. Reprinted with permission from [54]. © IOP Publishing.

Table 2. Evaluation results of CVs under noisy conditions. SD = standard deviation. Reprinted with permission from [54]. © IOP Publishing.

	T4P	**T2P**	**S4P**	**S2P**
CV: SD = 0.01	0.194	0.265	0.288	0.289
CV: SD = 0.05	0.722	0.830	0.839	0.869

3.3. Digital Spatial–Temporal Demodulation

In the early development of OSH, a lock-in amplifier was an essential instrument to extract the information in the heterodyne signal [68]. As high-performance computer and high-sampling rate analog-to-digital devices became cheaper, spatial–temporal demodulation was developed as an alternative demodulation method [69,70]. A diagram illustrating the flow of spatial–temporal demodulation is shown in Figure 13. Here, the raw data correspond to one hologram line, as shown in Figure 13a. The raw data are Fourier transformed to the spectrum domain (Figure 13b). The spectrum contains the zeroth order, the first order located at $\omega = \Omega$, which is the modulation angular frequency of EOM, and the negative order at $\omega = -\Omega$. Being similar to off-axis holography, the phase as well as the amplitude of the object's light are retained in the first order, and thus the first order, centered at the spectrum domain, is solely extracted (Figure 13c) and then inverse Fourier transformed to the time domain. It should be noted that the scanning time t and the hologram coordinate x satisfy the relationship $x = vt$, where v is the scanning speed. Therefore, the result of the inverse Fourier transform can be directly mapped to the spatial domain, as shown in Figure 13d. As the above processing is performed for all hologram lines, a complex hologram free from the zeroth order and the twin image is obtained and can be reconstructed using Equation (5). The spatial–temporal demodulation can also be applied to MOSH or IOSH, provided digital scanning is still performed with

the line-by-line scheme (i.e., raster scanning). In IOSH, the initial phase of each scanning line stays the same, and thus digital spatial–temporal demodulation can be performed by a single 2D Fourier transform, filtering, and a single 2D inverse Fourier transform [46]. Finally, the location of the first order depends on the number of steps for the phase shifting. For four-step phase shifting, the first order is located at $1/4\Delta$, where Δ is the pixel pitch of the hologram. In this case, the phase of FZP changes horizontally, and thus the bandwidth of the object light must be limited to less than half the horizontal sampling bandwidth, while the vertical sampling bandwidth can be fully utilized. As a comparison, only 1/2 bandwidth along both directions can be utilized in the SDPS method because of the division and interpolation.

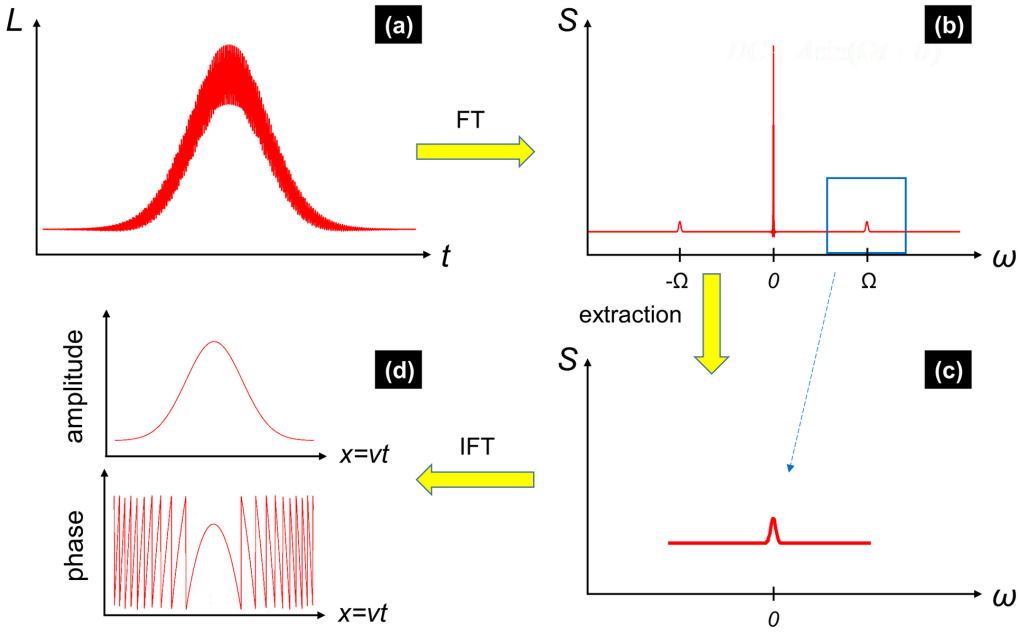

Figure 13. Flow diagram of one-dimensional spatial–temporal demodulation. (**a**) The raw hologram line L as a function of time t. (**b**) The Fourier spectrum S of (**a**). (**c**) The extracted spectrum. (**d**) The demodulated phase and amplitude of the hologram line. FT and IFT stand for the Fourier transform and inverse Fourier transform, respectively.

4. Applications

4.1. Quantitative Phase Imaging

The information related to the phase delay caused by an object is known to carry informative physical parameters such as the refractive index or thickness [71], scattering parameters [72], aberrations [73], molecular vibrations [74], and properties intrinsic to the object [75]. Quantitative phase imaging (QPI) methods enabling these capabilities are crucial in measurement technology, and various techniques have been proposed. In conventional OSH, acquired holograms are incoherent holograms, meaning an obtained phase distribution contains only information about the three-dimensional position of an object. The phase delay information caused by an object is not inherently present in incoherent holograms.

Methods for obtaining the quantitative phase distribution in OSH have been proposed, and this can be achieved by placing a pinhole in front of the detector [39–42]. These methods are called a coherent mode of OSH. By using a pinhole in front of a detector, the obtained hologram becomes a coherent hologram. This method has already been implemented in MOSH [76].

Implementing this method in MOSH has the advantage of being robust against disturbances such as vibrations, which were problematic in conventional interferometers as they were realized through a common path configuration. In [76], a principle validation experiment was conducted by placing a pinhole in front of the detector. A microlens array

was used as the measurement sample. The experimental results in Figure 14 demonstrate a consistent phase difference compared with an ideal spherical wave with the same focal length. The paper also explored verification using slide glass and microdot lenses, as mentioned in [76].

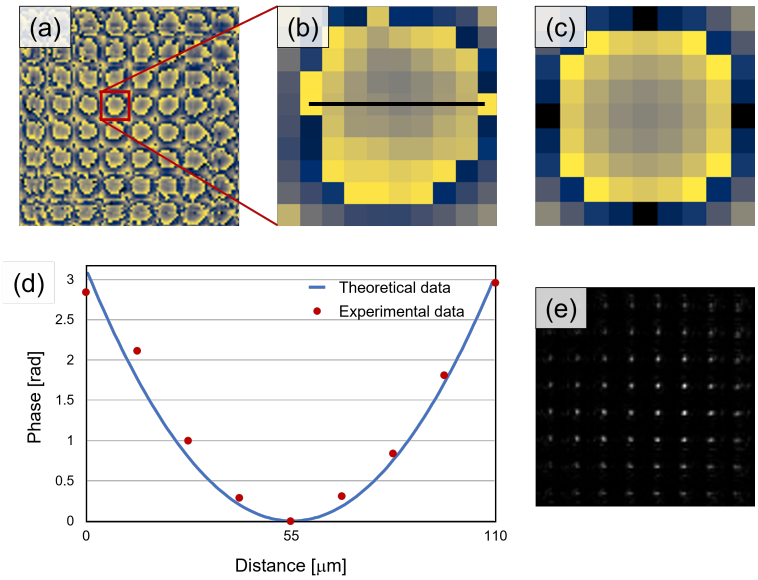

Figure 14. Experimental results of a microlens array: (**a**) phase distribution, (**b**) enlarged microlens, (**c**) theoretical microlens, (**d**) comparison of sectional profiles, and (**e**) reconstructed spot intensity distribution. Reprinted with permission from [76]. © Optica Publishing Group.

4.2. Imaging through Scattering Media

Scattering media, such as atmospheric disturbances, fog, and biological cells, disturb the propagation direction of light [77]. Visualizing through scattering media is essential in various fields like biology, medicine, astronomy, and optical communication. Scattering imaging has been proposed for this purpose by employing various techniques. Methods to measure the transmission matrix (TM) of scattering media [78,79] or point spread functions (PSFs) [80,81] have been suggested. However, obtaining such prior information is difficult in practical applications. Speckle correlation imaging, utilizing memory effects, is a noninvasive method, but iterative phase retrieval is required to obtain the primary object image, leading to issues like solution stagnation and non-unique solutions [82,83].

SPI, an imaging method which does not rely on conventional focusing, has been applied to scattering imaging, eliminating the need for prior information about the scattering medium and iterative phase retrieval [10,84–87]. The advantage of not requiring prior information about the scattering medium allows for imaging through scattering media, even when the scattering medium undergoes temporal changes [10]. While conventional SPI is effective when there is a scattering medium between the object and the detector, reconstructing images is generally challenging when there is a scattering medium between the illumination and the object. However, recent research has proposed methods to overcome this limitation [88]. In addition, SPI can obtain additional physical parameters such as the scattering and absorption coefficients [89].

In [90], the report discusses the visualization of three-dimensional objects behind scattering media using MOSH. The optical system of MOSH in Figure 4 was utilized in the experiments. The experimental results with fluorescent beads demonstrate the visualization of the region behind diffusive plates with scattering angles of 1, 5, 20, and 40 degrees, as shown in Figure 15.

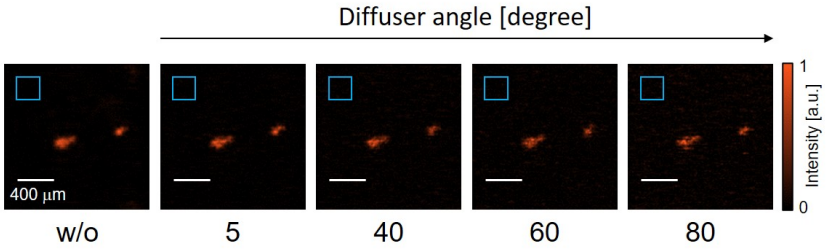

Figure 15. Reconstructed intensity distributions through static scattering media. The numbers at the bottom of the images represent the diffusion angle of the diffusers. Reprinted with permission from [90]. © AIP Publishing.

Additionally, experimental confirmation of three-dimensional incoherent object visualization was provided. The experimental set-up involved placing a fluorescent plate for microscope calibration and a USAF test target on top of each other, with an 8 mm distance from the beam splitter. The relationship of each component position is described in Figure 5 of [90]. The validation experiment tested whether the stationary diffusive plate and the dynamic diffusive plate's region beyond were visualized. The results are depicted in Figure 16, showing that MOSH can look through rotating scattering media, indicating its capability even when the scattering medium is dynamically changed.

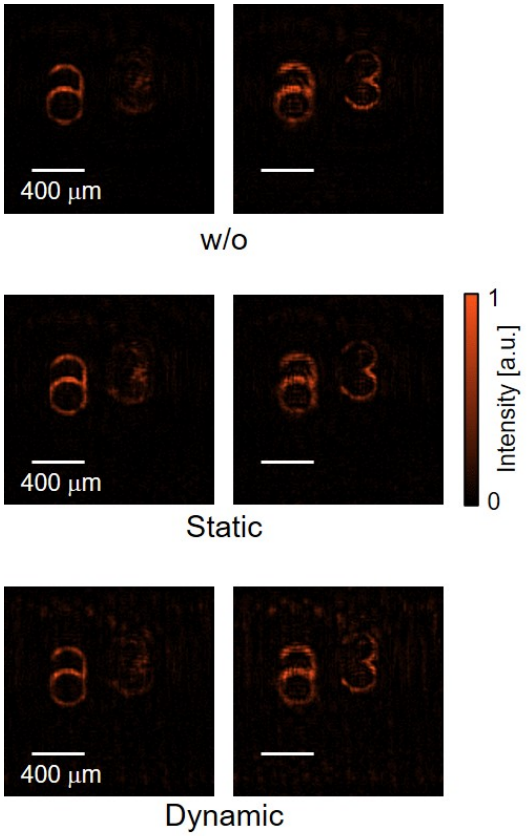

Figure 16. Reconstructed intensity distributions of 3D fluorescent object. The left and right columns indicate the focal planes of elements 6 and 3, respectively. Reprinted with permission from [90]. © AIP Publishing.

4.3. Polarization Imaging

One of the degrees of freedom of light is polarization. Research has been conducted to investigate the surface measurements [91], stress distribution [92], and molecular orientation in samples by acquiring polarization information [93,94]. If polarization imaging

can be realized in COSH, then it can expand the potential applications of OSH. The authors of [95] reported on polarization imaging under COSH. This method combines COSH with polarizer-rotating techniques. A polarizer is placed in front of the detector, and the transmission axis is rotated at 0, 45, 90, and 135 degrees to acquire complex holograms. The intensity distribution at any focal position is obtained through wave propagation calculations from the acquired complex holograms. By determining the Stokes parameters using the intensity distributions with each piece of polarization information, polarization imaging in OSH becomes possible.

Figure 17 illustrates the results of polarization imaging in COSH.

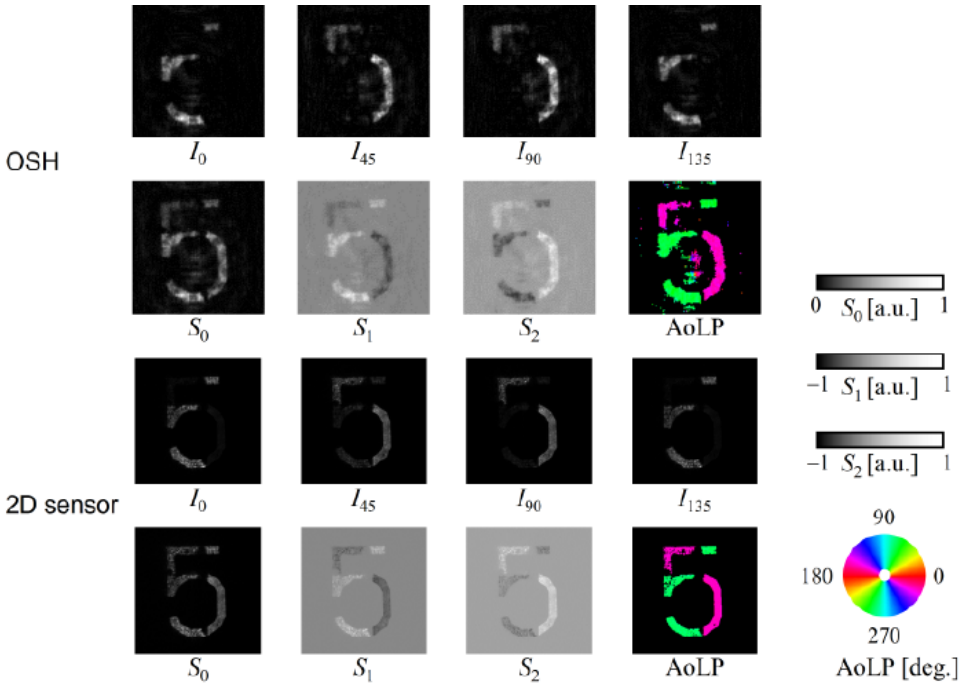

Figure 17. The experimental results. The upper and lower regions show the results of the proposed method and the image sensor, respectively. Reprinted with permission from [95]. © The Optical Society of Japan.

In this proof-of-principle experiment, a USAF test target overlaid with cellophane tape, being a birefringent object, was used. For comparison, images obtained using the polarizer-rotating technique are shown in the lower part of Figure 17.

The comparison between the results of COSH and a 2D image sensor demonstrates that polarization imaging is achievable in MOSH. Additionally, experiments were conducted by integrating scattered transmission imaging, as introduced in Section 3.2. The experimental results are presented in Figure 18. For comparison, the results obtained using the polarizer-rotating technique with an imaging sensor are shown in the lower part of Figure 18. These results indicate that MOSH can visualize the polarization distribution of the object through scattering media, which cannot be obtained with conventional polarizer-rotating techniques.

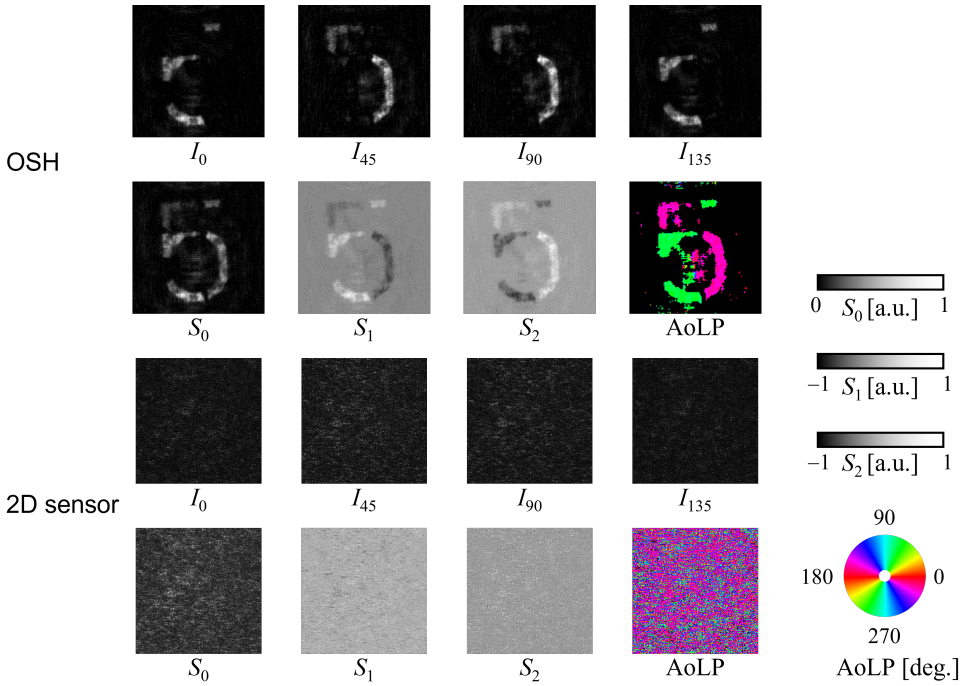

Figure 18. The results of polarization imaging through scattering media. Reprinted with permission from [95]. © The Optical Society of Japan.

5. Conclusions

In this review, we introduced the techniques of COSH, including MOSH and IOSH. In COSH, an LC-SLM or a DMD is applied in the system to realize both scanning and phase-shifting or heterodyning. Since the system was significantly simplified, not only the form factor but also the cost of the system can be reduced in comparison with the conventional OSH. Three applications were introduced in this review. These are not diverse research directions as solutions to the problems in the respective fields through the OSH system. Rather, they are at the stage of showing that these applications are achievable via the OSH system. In the future, when the OSH system can be used for applications that cannot be achieved with other holographic systems, it will be useful to show that these applications are also possible with the COSH system. The limitations of these applications under COSH include the need for structured illumination, because of OSH being one of the SPI techniques and the limited imaging speed due to single-pixel detection. The main challenge of COSH is the limited space–bandwidth product (SBP) of the digital device; aliasing is easily observed in COSH. Aside from that, the hologram size and the resolution are also worse due to the limited SBP. Nevertheless, COSH has proven its great potential because of its unique features, as we revealed in this paper. We believe COSH will find irreplaceable applications soon.

Author Contributions: Conceptualization, N.Y. and J.-P.L.; methodology, N.Y. and J.-P.L.; validation, N.Y. and J.-P.L.; formal analysis, N.Y. and J.-P.L.; investigation, N.Y. and J.-P.L.; resources, N.Y., J.-P.L., O.M., Y.S. and T.N.; data curation, N.Y. and J.-P.L.; writing—original draft preparation, N.Y. and J.-P.L.; writing—review and editing, O.M., Y.S. and T.N.; visualization, N.Y. and J.-P.L.; supervision, T.N.; project administration, J.-P.L., O.M. and T.N.; funding acquisition, N.Y., J.-P.L., O.M. and T.N. All authors have read and agreed to the published version of the manuscript.

Funding: A part of this research was supported by JSPS KAKENHI (20H05886, 21H04663, 23K13680) and the National Science and Technology Council of Taiwan (109-2221-E-035-076-MY3, 112-2221-E-035-070-MY3).

Institutional Review Board Statement: Not applicable.

Informed Consent Statement: Not applicable.

Data Availability Statement: Data underlying the results presented in this paper are not publicly available at this time but may be obtained from the authors upon reasonable request.

Conflicts of Interest: The authors declare no conflicts of interest.

Abbreviations

The following abbreviations are used in this manuscript:

OSH	Optical scanning holography
MOSH	Motionless optical scanning holography
IOSH	Interferenceless optical scanning holography
COSH	Computational optical scanning holography
SLM	Spatial light modulator
GI	Ghost imaging
CGI	Computational ghost imaging
HTI	Hadamard transform imaging
FSI	Fourier single-pixel imaging
IDH	Incoherent digital holography
CV	Coefficient of variance
SDPS	Spatially divided phase shifting
SBP	Space–bandwidth product

References

1. Mait, J.N.; Euliss, G.W.; Athale, R.A. Computational imaging. *Adv. Opt. Photon.* **2018**, *10*, 409–483. [CrossRef]
2. Gibson, G.M.; Johnson, S.D.; Padgett, M.J. Single-pixel imaging 12 years on: A review. *Opt. Express* **2020**, *28*, 28190–28208. [CrossRef] [PubMed]
3. Radwell, N.; Mitchell, K.J.; Gibson, G.M.; Edgar, M.P.; Bowman, R.; Padgett, M.J. Single-pixel infrared and visible microscope. *Optica* **2014**, *1*, 285–289. [CrossRef]
4. Yu, H.; Lu, R.; Han, S.; Xie, H.; Du, G.; Xiao, T.; Zhu, D. Fourier-Transform Ghost Imaging with Hard X Rays. *Phys. Rev. Lett.* **2016**, *117*, 113901. [CrossRef] [PubMed]
5. Gibson, G.M.; Sun, B.; Edgar, M.P.; Phillips, D.B.; Hempler, N.; Maker, G.T.; Malcolm, G.P.A.; Padgett, M.J. Real-time imaging of methane gas leaks using a single-pixel camera. *Opt. Express* **2017**, *25*, 2998–3005. [CrossRef] [PubMed]
6. Vallés, A.; He, J.; Ohno, S.; Omatsu, T.; Miyamoto, K. Broadband high-resolution terahertz single-pixel imaging. *Opt. Express* **2020**, *28*, 28868–28881. [CrossRef] [PubMed]
7. Olivieri, L.; Gongora, J.S.T.; Peters, L.; Cecconi, V.; Cutrona, A.; Tunesi, J.; Tucker, R.; Pasquazi, A.; Peccianti, M. Hyperspectral terahertz microscopy via nonlinear ghost imaging. *Optica* **2020**, *7*, 186–191. [CrossRef]
8. Liu, X.; Shi, J.; Sun, L.; Li, Y.; Fan, J.; Zeng, G. Photon-limited single-pixel imaging. *Opt. Express* **2020**, *28*, 8132–8144. [CrossRef] [PubMed]
9. Shibuya, K.; Araki, H.; Iwata, T. Photon-counting-based diffraction phase microscopy combined with single-pixel imaging. *Jpn. J. Appl. Phys.* **2018**, *57*, 042501. [CrossRef]
10. Tajahuerce, E.; Durán, V.; Clemente, P.; Irles, E.; Soldevila, F.; Andrés, P.; Lancis, J. Image transmission through dynamic scattering media by single-pixel photodetection. *Opt. Express* **2014**, *22*, 16945–16955. [CrossRef]
11. Yang, X.; Liu, Y.; Mou, X.; Hu, T.; Yuan, F.; Cheng, E. Imaging in turbid water based on a Hadamard single-pixel imaging system. *Opt. Express* **2021**, *29*, 12010–12023. [CrossRef] [PubMed]
12. Pittman, T.B.; Shih, Y.H.; Strekalov, D.V.; Sergienko, A.V. Optical imaging by means of two-photon quantum entanglement. *Phys. Rev. A* **1995**, *52*, R3429–R3432. [CrossRef] [PubMed]
13. Shapiro, J.H. Computational ghost imaging. *Phys. Rev. A* **2008**, *78*, 061802. [CrossRef]
14. Pratt, W.; Kane, J.; Andrews, H. Hadamard transform image coding. *Proc. IEEE* **1969**, *57*, 58–68. [CrossRef]
15. Zhang, Z.; Ma, X.; Zhong, J. Single-pixel imaging by means of Fourier spectrum acquisition. *Nat. Commun.* **2015**, *6*, 6225. [CrossRef] [PubMed]
16. Poon, T.C.; Korpel, A. Optical transfer function of an acousto-optic heterodyning image processor. *Opt. Lett.* **1979**, *4*, 317. [CrossRef] [PubMed]
17. Poon, T.C. *Optical Scanning Holography with MATLAB®*; Springer: Berlin/Heidelberg, Germany , 2007. [CrossRef]
18. Kim, H.; Kim, Y.S.; Kim, T. Full-color optical scanning holography with common red, green, and blue channels [Invited]. *Appl. Opt.* **2016**, *55*, A17–A21. [CrossRef] [PubMed]
19. Xin, Z.; Dobson, K.; Shinoda, Y.; Poon, T.C. Sectional image reconstruction in optical scanning holography using a random-phase pupil. *Opt. Lett.* **2010**, *35*, 2934–2936. [CrossRef] [PubMed]
20. Wu, X.L.; Zhou, X.; Wang, Q.H.; Jiang, Y.F.; Xiao, C.J.; Dobson, K.; Poon, T.C. Deviation influences on sectional image reconstruction in optical scanning holography using a random-phase pupil. *Appl. Opt.* **2013**, *52*, A360–A366. [CrossRef]

21. Ou, H.; Poon, T.C.; Wong, K.K.Y.; Lam, E.Y. Enhanced depth resolution in optical scanning holography using a configurable pupil. *Photon. Res.* **2014**, *2*, 64–70. [CrossRef]
22. Zhang, Y.; Wang, R.; Tsang, P.; Poon, T.C. Sectioning with edge extraction in optical incoherent imaging processing. *OSA Contin.* **2020**, *3*, 698–708. [CrossRef]
23. Liu, J.P.; Wang, S.Y. Stereo-Lighting Reconstruction of Optical Scanning Holography. *IEEE Trans. Ind. Informatics* **2016**, *12*, 1664–1669. [CrossRef]
24. Pan, Y.; Jia, W.; Yu, J.; Dobson, K.; Zhou, C.; Wang, Y.; Poon, T.C. Edge extraction using a time-varying vortex beam in incoherent digital holography. *Opt. Lett.* **2014**, *39*, 4176–4179. [CrossRef] [PubMed]
25. Ou, H.; Wu, Y.; Lam, E.Y.; Wang, B.Z. Axial localization using time reversal multiple signal classification in optical scanning holography. *Opt. Express* **2018**, *26*, 3756–3771. [CrossRef]
26. Chang, X.; Yan, A.; Zhang, H. Ciphertext-only attack on optical scanning cryptography. *Opt. Lasers Eng.* **2020**, *126*, 105901. [CrossRef]
27. Ren, Z.; Lam, E.Y. Super-resolution imaging in optical scanning holography using structured illumination. In Proceedings of the Holography, Diffractive Optics, and Applications VII, Beijing, China, 12–14 October 2016; Sheng, Y., Yu, C., Zhou, C., Eds.; International Society for Optics and Photonics, SPIE: Bellingham, WA, USA, 2016; Volume 10022, p. 1002203. [CrossRef]
28. Chen, N.; Ren, Z.; Ou, H.; Lam, E.Y. Resolution enhancement of optical scanning holography with a spiral modulated point spread function. *Photon. Res.* **2016**, *4*, 1–6. [CrossRef]
29. Kim, T.; Poon, T.C.; Indebetouw, G.J.M. Depth detection and image recovery in remote sensing by optical scanning holography. *Opt. Eng.* **2002**, *41*, 1331–1338. [CrossRef]
30. Liu, J.P.; Tahara, T.; Hayasaki, Y.; Poon, T.C. Incoherent Digital Holography: A Review. *Appl. Sci.* **2018**, *8*, 143. [CrossRef]
31. Yoneda, N.; Ipus, E.; Ordóñez, L.; Lenz, A.J.M.; Martínez-León, L.; Matoba, O.; Tajahuerce, E. Videography based on computational optical scanning holography. In Proceedings of the Optica Imaging Congress (3D, COSI, DH, FLatOptics, IS, pcAOP), Boston, MA, USA, 14–17 August 2023; Optica Publishing Group: Washington, DC, USA, 2023; p. HM4C.8. [CrossRef]
32. Yu, H.; Kim, Y.; Yang, D.; Seo, W.; Kim, Y.; Hong, J.Y.; Song, H.; Sung, G.; Sung, Y.; Min, S.W.; et al. Deep learning-based incoherent holographic camera enabling acquisition of real-world holograms for holographic streaming system. *Nat. Commun.* **2023**, *14*, 3534. [CrossRef] [PubMed]
33. Muroi, T.; Nobukawa, T.; Katano, Y.; Hagiwara, K. Capturing videos at 60 frames per second using incoherent digital holography. *Opt. Contin.* **2023**, *2*, 2409–2420. [CrossRef]
34. Tahara, T.; Shimobaba, T. High-speed phase-shifting incoherent digital holography (invited). *Appl. Phys. B* **2023**, *129*, 96. [CrossRef]
35. Tsang, P.W.M.; Liu, J.P.; Poon, T.C. Compressive optical scanning holography. *Optica* **2015**, *2*, 476–483. [CrossRef]
36. Chan, A.C.S.; Tsia, K.K.; Lam, E.Y. Subsampled scanning holographic imaging (SuSHI) for fast, non-adaptive recording of three-dimensional objects. *Optica* **2016**, *3*, 911–917. [CrossRef]
37. Tsang, P.W.M.; Poon, T.C.; Liu, J.P. Adaptive Optical Scanning Holography. *Sci. Rep.* **2016**, *6*, 21636. [CrossRef] [PubMed]
38. Tsang, P.W.M.; Poon, T.C.; Liu, J.P.; Kim, T.; Kim, Y.S. Low Complexity Compression and Speed Enhancement for Optical Scanning Holography. *Sci. Rep.* **2016**, *6*, 34724. [CrossRef]
39. Indebetouw, G.; Klysubun, P.; Kim, T.; Poon, T.C. Imaging properties of scanning holographic microscopy. *J. Opt. Soc. Am. A* **2000**, *17*, 380–390. [CrossRef]
40. Indebetouw, G.; Tada, Y.; Leacock, J. Quantitative phase imaging with scanning holographic microscopy: An experimental assesment. *Biomed. Eng. Online* **2006**, *5*, 63. [CrossRef] [PubMed]
41. Liu, J.P. Spatial coherence analysis for optical scanning holography. *Appl. Opt.* **2015**, *54*, A59–A66. [CrossRef] [PubMed]
42. Liu, J.P.; Guo, C.H.; Hsiao, W.J.; Poon, T.C.; Tsang, P. Coherence experiments in single-pixel digital holography. *Opt. Lett.* **2015**, *40*, 2366–2369. [CrossRef]
43. Kim, T.; Kim, T. Coaxial scanning holography. *Opt. Lett.* **2020**, *45*, 2046–2049. [CrossRef]
44. Tsai, C.M.; Sie, H.Y.; Poon, T.C.; Liu, J.P. Optical scanning holography with a polarization directed flat lens. *Appl. Opt.* **2021**, *60*, B113–B118. [CrossRef] [PubMed]
45. Yoneda, N.; Saita, Y.; Nomura, T. Motionless optical scanning holography. *Opt. Lett.* **2020**, *45*, 3184–3187. [CrossRef] [PubMed]
46. Liu, J.P.; Tsai, C.M.; Poon, T.C.; Tsang, P.; Zhang, Y. Three-dimensional imaging by interferenceless optical scanning holography. *Opt. Lasers Eng.* **2022**, *158*, 107183. [CrossRef]
47. Shinoda, Y.; Liu, J.P.; Chung, P.S.; Dobson, K.; Zhou, X.; Poon, T.C. Three-dimensional complex image coding using a circular Dammann grating. *Appl. Opt.* **2011**, *50*, B38–B45. [CrossRef] [PubMed]
48. Liu, J.P.; Lee, C.C.; Lo, Y.H.; Luo, D.Z. Vertical-bandwidth-limited digital holography. *Opt. Lett.* **2012**, *37*, 2574–2576. [CrossRef] [PubMed]
49. Zhang, L.Z.; Zhou, X.; Wang, D.; Li, N.N.; Bai, X.; Wang, Q.H. Multiple-image encryption based on optical scanning holography using orthogonal compressive sensing and random phase mask. *Opt. Eng.* **2020**, *59*, 102411. [CrossRef]
50. Zhang, Y.; Poon, T.C.; Tsang, P.W.M.; Wang, R.; Wang, L. Review on Feature Extraction for 3-D Incoherent Image Processing Using Optical Scanning Holography. *IEEE Trans. Ind. Inform.* **2019**, *15*, 6146–6154. [CrossRef]
51. Swoger, J.; Martinez-Corral, M.; Huisken, J.; Stelzer, E.H.K. Optical scanning holography as a technique for high-resolution three-dimensional biological microscopy. *J. Opt. Soc. Am. A* **2002**, *19*, 1910–1918. [CrossRef] [PubMed]

52. Rosen, J.; Brooker, G. Digital spatially incoherent Fresnel holography. *Opt. Lett.* **2007**, *32*, 912–914. [CrossRef]
53. Takasaki, H.; Yoshino, Y. Polarization Interferometer. *Appl. Opt.* **1969**, *8*, 2344–2345. [CrossRef]
54. Yoneda, N.; Saita, Y.; Nomura, T. Spatially divided phase-shifting motionless optical scanning holography. *OSA Contin.* **2020**, *3*, 3523–3535. [CrossRef]
55. Tsang, P.; Poon, T.C. Non-diffractive Optical Scanning Holography for Hologram Acquisition. In Proceedings of the Digital Holography and Three-Dimensional Imaging 2019, Bordeaux, France, 19–23 May 2019; Optica Publishing Group: Washington, DC, USA, 2019; p. Th1B.6. [CrossRef]
56. Nomura, T.; Shinomura, K. Generalized sequential four-step phase-shifting color digital holography. *Appl. Opt.* **2017**, *56*, 6851–6854. [CrossRef]
57. Awatsuji, Y.; Sasada, M.; Kubota, T. Parallel quasi-phase-shifting digital holography. *Appl. Phys. Lett.* **2004**, *85*, 1069–1071. [CrossRef]
58. Awatsuji, Y.; Tahara, T.; Kaneko, A.; Koyama, T.; Nishio, K.; Ura, S.; Kubota, T.; Matoba, O. Parallel two-step phase-shifting digital holography. *Appl. Opt.* **2008**, *47*, D183–D189. [CrossRef]
59. Tahara, T.; Ito, K.; Kakue, T.; Fujii, M.; Shimozato, Y.; Awatsuji, Y.; Nishio, K.; Ura, S.; Kubota, T.; Matoba, O. Parallel phase-shifting digital holographic microscopy. *Biomed. Opt. Express* **2010**, *1*, 610–616. [CrossRef]
60. Yoneda, N.; Quan, X.; Matoba, O. Single-shot generalized Hanbury Brown & Twiss experiments using a polarization camera for target intensity reconstruction in scattering media. *Opt. Lett.* **2023**, *48*, 632–635. [CrossRef]
61. Kakue, T.; Yonesaka, R.; Tahara, T.; Awatsuji, Y.; Nishio, K.; Ura, S.; Kubota, T.; Matoba, O. High-speed phase imaging by parallel phase-shifting digital holography. *Opt. Lett.* **2011**, *36*, 4131–4133. [CrossRef]
62. Takase, Y.; Shimizu, K.; Mochida, S.; Inoue, T.; Nishio, K.; Rajput, S.K.; Matoba, O.; Xia, P.; Awatsuji, Y. High-speed imaging of the sound field by parallel phase-shifting digital holography. *Appl. Opt.* **2021**, *60*, A179–A187. [CrossRef]
63. Yoneda, N.; Matoba, O. Two-Step Phase-Shifting Motionless Optical Scanning Holography. In Proceedings of the Imaging and Applied Optics Congress 2022 (3D, AOA, COSI, ISA, pcAOP), Vancouver, BC, Canada, 11–15 July 2022; Optica Publishing Group: Washington, DC, USA, 2022; p. 3F3A.7. [CrossRef]
64. Yoneda, N.; Matoba, O. Spatially divided two-step phase-shifting method for computational optical scanning holography. *J. Opt.* **2023**, *25*, 124001. [CrossRef]
65. Meng, X.F.; Cai, L.Z.; Xu, X.F.; Yang, X.L.; Shen, X.X.; Dong, G.Y.; Wang, Y.R. Two-step phase-shifting interferometry and its application in image encryption. *Opt. Lett.* **2006**, *31*, 1414–1416. [CrossRef]
66. Liu, J.P.; Poon, T.C. Two-step-only quadrature phase-shifting digital holography. *Opt. Lett.* **2009**, *34*, 250–252. [CrossRef]
67. Tahara, T.; Kozawa, Y.; Ishii, A.; Wakunami, K.; Ichihashi, Y.; Oi, R. Two-step phase-shifting interferometry for self-interference digital holography. *Opt. Lett.* **2021**, *46*, 669–672. [CrossRef]
68. Poon, T.C.; Kim, T.; Indebetouw, G.; Schilling, B.W.; Wu, M.H.; Shinoda, K.; Suzuki, Y. Twin-image elimination experiments for three-dimensional images in optical scanning holography. *Opt. Lett.* **2000**, *25*, 215–217. [CrossRef]
69. Indebetouw, G.; Zhong, W. Scanning holographic microscopy of three-dimensional fluorescent specimens. *J. Opt. Soc. Am. A* **2006**, *23*, 1699–1707. [CrossRef]
70. Liu, J.P.; Luo, D.Z.; Lu, S.H. Spatial–temporal demodulation technique for heterodyne optical scanning holography. *Opt. Lasers Eng.* **2015**, *68*, 42–49. [CrossRef]
71. Muñoz, V.H.F.; Arellano, N.I.T.; García, D.I.S.; García, A.M.; Zurita, G.R.; Lechuga, L.G. Measurement of mean thickness of transparent samples using simultaneous phase shifting interferometry with four interferograms. *Appl. Opt.* **2016**, *55*, 4047–4051. [CrossRef]
72. Takabayashi, M.; Majeed, H.; Kajdacsy-Balla, A.; Popescu, G. Disorder strength measured by quantitative phase imaging as intrinsic cancer marker in fixed tissue biopsies. *PLoS ONE* **2018**, *13*, e0194320. [CrossRef]
73. Choi, I.; Lee, K.; Park, Y. Compensation of aberration in quantitative phase imaging using lateral shifting and spiral phase integration. *Opt. Express* **2017**, *25*, 30771–30779. [CrossRef]
74. Tamamitsu, M.; Toda, K.; Horisaki, R.; Ideguchi, T. Quantitative phase imaging with molecular vibrational sensitivity. *Opt. Lett.* **2019**, *44*, 3729–3732. [CrossRef]
75. Ma, Y.; Dai, T.; Lei, Y.; Zheng, J.; Liu, M.; Sui, B.; Smith, Z.J.; Chu, K.; Kong, L.; Gao, P. Label-free imaging of intracellular organelle dynamics using flat-fielding quantitative phase contrast microscopy (FF-QPCM). *Opt. Express* **2022**, *30*, 9505–9520. [CrossRef]
76. Yoneda, N.; Matoba, O.; Saita, Y.; Nomura, T. Quantitative phase imaging based on motionless optical scanning holography. *Opt. Lett.* **2023**, *48*, 5273–5276. [CrossRef]
77. Rotter, S.; Gigan, S. Light fields in complex media: Mesoscopic scattering meets wave control. *Rev. Mod. Phys.* **2017**, *89*, 015005. [CrossRef]
78. Popoff, S.M.; Lerosey, G.; Carminati, R.; Fink, M.; Boccara, A.C.; Gigan, S. Measuring the Transmission Matrix in Optics: An Approach to the Study and Control of Light Propagation in Disordered Media. *Phys. Rev. Lett.* **2010**, *104*, 100601. [CrossRef]
79. Kim, M.; Choi, W.; Choi, Y.; Yoon, C.; Choi, W. Transmission matrix of a scattering medium and its applications in biophotonics. *Opt. Express* **2015**, *23*, 12648–12668. [CrossRef]
80. Li, L.; Li, Q.; Sun, S.; Lin, H.Z.; Liu, W.T.; Chen, P.X. Imaging through scattering layers exceeding memory effect range with spatial-correlation-achieved point-spread-function. *Opt. Lett.* **2018**, *43*, 1670–1673. [CrossRef]

81. Wu, T.; Dong, J.; Gigan, S. Non-invasive single-shot recovery of a point-spread function of a memory effect based scattering imaging system. *Opt. Lett.* **2020**, *45*, 5397–5400. [CrossRef]
82. Bertolotti, J.; van Putten, E.G.; Blum, C.; Lagendijk, A.; Vos, W.L.; Mosk, A.P. Non-invasive imaging through opaque scattering layers. *Nature* **2012**, *491*, 232–234. [CrossRef]
83. Liao, M.; Lu, D.; He, W.; Pedrini, G.; Osten, W.; Peng, X. Improving reconstruction of speckle correlation imaging by using a modified phase retrieval algorithm with the number of nonzero-pixels constraint. *Appl. Opt.* **2019**, *58*, 473–478. [CrossRef]
84. Durán, V.; Soldevila, F.; Irles, E.; Clemente, P.; Tajahuerce, E.; Andrés, P.; Lancis, J. Compressive imaging in scattering media. *Opt. Express* **2015**, *23*, 14424–14433. [CrossRef]
85. Martínez-León, L.; Clemente, P.; Mori, Y.; Climent, V.; Lancis, J.; Tajahuerce, E. Single-pixel digital holography with phase-encoded illumination. *Opt. Express* **2017**, *25*, 4975–4984. [CrossRef]
86. Dutta, R.; Manzanera, S.; Gambín-Regadera, A.; Irles, E.; Tajahuerce, E.; Lancis, J.; Artal, P. Single-pixel imaging of the retina through scattering media. *Biomed. Opt. Express* **2019**, *10*, 4159–4167. [CrossRef]
87. Paniagua-Diaz, A.M.; Starshynov, I.; Fayard, N.; Goetschy, A.; Pierrat, R.; Carminati, R.; Bertolotti, J. Blind ghost imaging. *Optica* **2019**, *6*, 460–464. [CrossRef]
88. Zhao, S.; Rauer, B.; Valzania, L.; Dong, J.; Liu, R.; Li, F.; Gigan, S.; de Aguiar, H.B. Single-pixel transmission matrix recovery via two-photon fluorescence. *Sci. Adv.* **2024**, *10*, eadi3442. [CrossRef]
89. Lenz, A.J.M.; Clemente, P.; Climent, V.; Lancis, J.; Tajahuerce, E. Imaging the optical properties of turbid media with single-pixel detection based on the Kubelka–Munk model. *Opt. Lett.* **2019**, *44*, 4797–4800. [CrossRef]
90. Yoneda, N.; Saita, Y.; Nomura, T. Three-dimensional fluorescence imaging through dynamic scattering media by motionless optical scanning holography. *Appl. Phys. Lett.* **2021**, *119*, 161101. [CrossRef]
91. Garcia, N.M.; de Erausquin, I.; Edmiston, C.; Gruev, V. Surface normal reconstruction using circularly polarized light. *Opt. Express* **2015**, *23*, 14391–14406. [CrossRef] [PubMed]
92. Bei, C.; Xuejie, Z.; Cheng, L.; Zhu, J. Full-field stress measurement based on polarization ptychography. *J. Opt.* **2019**, *21*, 065602. [CrossRef]
93. Garcia, M.; Davis, T.; Blair, S.; Cui, N.; Gruev, V. Bioinspired polarization imager with high dynamic range. *Optica* **2018**, *5*, 1240–1246. [CrossRef]
94. Mehta, S.B.; McQuilken, M.; Riviere, P.J.L.; Occhipinti, P.; Verma, A.; Oldenbourg, R.; Gladfelter, A.S.; Tani, T. Dissection of molecular assembly dynamics by tracking orientation and position of single molecules in live cells. *Proc. Natl. Acad. Sci. USA* **2016**, *113*, E6352–E6361. [CrossRef]
95. Yoneda, N.; Saita, Y.; Nomura, T. Polarization imaging by use of optical scanning holography. *Opt. Rev.* **2023**, *30*, 26–32. [CrossRef]